Remote Sensing of Environment 236 (2020) 111426

Contents lists available at ScienceDirect

Remote Sensing of Environment

journal homepage: www.elsevier.com/locate/rse

How the variety of satellite remote sensing data over volcanoes can assist hazard monitoring efforts: The 2011 eruption of Nabro volcano

Gaetana Ganci*, Annalisa Cappello, Giuseppe Bilotta, Ciro Del Negro

Istituto Nazionale di Geofisica e Vulcanologia, Sezione di Catania, Osservatorio Etneo, Catania, Italy

ARTICLE INFO

Keywords:
Lav@Hazard
HOTSAT
MAGFLOW
Satellite remote sensing
Numerical modelling

ABSTRACT

Satellite remote sensing is becoming an increasingly essential component of volcano monitoring, especially at little-known and remote volcanoes where in-situ measurements are unavailable and/or impractical. Moreover the synoptic view captured by satellite imagery over volcanoes can benefit hazard monitoring efforts. By monitoring, we mean both following the changing styles and intensities of the eruption once it has started, as well as nowcasting and eventually forecasting the areas potentially threatened by hazardous phenomena in an eruptive scenario. Here we demonstrate how the diversity of remote sensing data over volcanoes and the mutual interconnection between satellite observations and numerical simulations can improve lava flow hazard monitoring in response to effusive eruption. Time-averaged discharge rates (TADRs) obtained from low spatial/high temporal resolution satellite data (e.g. MODIS, SEVIRI) are complemented, compared and fine-tuned with detailed maps of volcanic deposits with the aim of constraining the conversion from satellite-derived radiant heat flux to TADR. Maps of volcanic deposits include the time-varying evolution of lava flow emplacement derived from multispectral satellite data (e.g. EO-ALI, Landsat, Sentinel-2, ASTER), as well as the flow thickness variations, retrieved from the topographic monitoring by using stereo or tri-stereo optical data (e.g. Pléiades, PlanetScope, ASTER). Finally, satellite-derived parameters are used as input and validation tags for the numerical modelling of lava flow scenarios. Our strategy is applied to the first historic eruption of Nabro volcano (Eritrea), occurred in June 2011. This eruptive event was characterized by the extraordinary quantity of SO_2 emitted into the atmosphere and the extent of the long lava flows, which had a significant impact on the inhabitants of the Eritrea-Ethiopia border region despite the low population density. Because of its remote position, little was known about this eruption regarding the quantity of volcanic deposits and the timing and mechanisms of their emplacement. We found that the total volume of deposits, calculated from differences of digital elevation models (DEMs), is about 580×10^6 m^3, of which about 336×10^6 m^3 is the volume of the main lava flow that advanced eastward beyond the caldera. Multi-spectral satellite observations indicate that the main lava flow had reached its maximum extent (~16 km) within about 4 days of the eruption onset on midnight 12 June. Lava flow simulations driven by satellite-derived parameters allow building an understanding of the advance rate and maximum extent of the main lava flow showing that it is likely to have reached 10.5 km in one day with a maximum speed of ~0.44 km/h.

1. Introduction

The integration of satellite remote sensing techniques and lava flow forecasting models represents a step towards the next generation of quantitative hazard assessment in response to effusive volcano eruptions (Del Negro et al., 2016). This is of paramount importance especially for remote volcanoes where in-situ measurements are difficult-to-impractical (Spampinato et al., 2013; Cappello et al., 2016a). Infrared remote sensing satellites (e.g. MSG-SEVIRI, EOS-MODIS) provide an effective means to derive an estimation of the effusion rate (Ganci et al., 2011b), one of the most important input parameters controlling the output of lava flow models (Bilotta et al., 2012). Physics-based models driven by satellite-derived parameters are capable of fast and accurate forecasts of lava flow inundation scenarios (Herault et al., 2009). Therefore we implemented a Web–geographic information system (GIS) framework, named Lav@Hazard, which merges the estimates of the satellite-derived time averaged discharge rate (TADR, i.e., the average effusion rate over a specified period) with computer simulations of lava flow paths (Ganci et al., 2012). This satellite-driven modeling strategy was successively applied to several volcanoes worldwide for

* Corresponding author.
E-mail address: gaetana.ganci@ingv.it (G. Ganci).

https://doi.org/10.1016/j.rse.2019.111426
Received 31 May 2019; Received in revised form 12 September 2019; Accepted 14 September 2019

quantifying lava flow hazards in response to effusive eruption (e.g. Vicari et al., 2009, 2011a; Scifoni et al., 2010; Kerestzuri et al., 2014; Cappello et al., 2016b). The accuracy of this strategy, especially in poorly monitored volcanoes, has been limited by: (i) the reliability of the conversion from the radiant heat flux, derived from multi-spectral satellite images, to TADR (e.g., Harris et al., 2007; Ganci et al., 2012); (ii) the opportunity for an on-line validation of simulated flow paths against the actual ones.

The radiant heat flux can be measured from satellite data with a certain percentage of error (e.g. 30%; Wooster et al., 2003), while the proportionality constant for the conversion to TADR is case specific and highly variable (Harris et al., 2010). Recently, a conversion constant called "radiant density" has been provided for several volcanoes worldwide (Coppola et al., 2013), introducing a formulation very sensitive to the silica content of the erupted lava bodies. According to this formulation, by considering only basic lavas, a silica content variation from 46.5 to 49 wt% (e.g. Corsaro and Pompilio, 2004) produces a total variation in the TADR of about 72%, more than the generally accepted satellite-derived error of 50% (Harris et al., 2007). However, regardless of the relationship between thermal emissions of lava flows and TADR, massive over/under-estimations can be found when comparing volume estimates retrieved from satellite thermal data with topographic mapping over volcanoes (e.g. Di Traglia et al., 2018; Zaksek et al., 2015; Bagnardi et al., 2016; Cappello et al., 2016a).

Initial attempts at on-line validation of simulated lava flow paths have been performed by using multispectral satellite data from polar-orbiting sensors (e.g. EO-ALI, Landsat) that provide locations of the active volcanic features, lengths, areas and radiant flux distribution of the actual flow fields (Del Negro et al., 2016; Cappello et al., 2016, 2019); however, this data does not provide information on the thickness distribution of the volcanic deposits.

One possible and relatively simple means of gaining insights in the conversion from satellite-derived radiant heat flux to TADR, as well as in the three-dimensional validation of simulated scenarios, is the topographic monitoring of the lava flow field evolution. This volume-based method can provide intra-eruptive bulk estimates of the lava emplacement by differencing syn-eruptive and pre-eruptive digital elevation models.

Topographic monitoring of lava flow fields by means of LIDAR (Neri et al., 2008; Fornaciai et al., 2010), laser scanner (Slatcher et al., 2015), Unmanned Aerial Vehicles (Turner et al., 2017; Favalli et al., 2018) and helicopter (Neri et al., 2017), has been proven to be very effective and precise in detecting and quantifying erupted products and morphological variations (Muller et al., 2017; Darmawan et al., 2018), even if these approaches are often impractical, especially in remote volcanoes, or when a large area is affected by changes due to eruptive events. An alternative is offered by optical satellites in multi-view configuration (e.g. Pléiades, PlanetScope); these can be used to generate multi-temporal topographic mapping (Bagnardi et al., 2016; Di Traglia et al., 2018; Ghuffar, 2018; Ganci et al., 2018, Ganci et al., 2019; 2019b) and are getting easier to obtain, often at low cost, even if their use is hindered by clouds, especially volcanic clouds, that can partially or totally obscure the target area.

Here we present an extension to the Lav@Hazard satellite-driven modeling strategy that combines a variety of satellite data (Table 1) with the objective of facilitating mutual feedback between satellite-derived source terms and accurate physical models, thus improving the overall quality of lava flow hazard assessment. In particular, we show how high and very high spatial resolution optical satellite data (e.g. Pléiades, PlanetScope, ASTER) can be used to complement and refine the mass flux rates derived from low spatial/high temporal resolution multispectral thermal data (e.g. MODIS, SEVIRI) and validate the simulation results. Higher spatial/lower temporal resolution satellite data (e.g. EO-ALI, Landsat, Sentinel-2), useful to detect active and cooling lava flow fields, are considered as further validation of the simulation results.

This improved strategy is applied to the 2011 eruption of Nabro volcano, which was mainly documented by multispectral satellite imagery; moreover, since this is a voluminous eruption (0.47 km^3; Goitom et al., 2015) with a magnitude of 5.1, we have been able to constrain the lava volume exploiting freely available optical satellite data. By using the dual view provided by ASTER data, we derived the pre-eruptive DEM and, thanks to the multi-view of PlanetScope images, we built the post-eruptive DEM. By differencing these two DEMs, we produced a three dimensional map of volcanic deposits. This map was used both to constrain the satellite-derived TADR curves, given as input to the lava flow model, and for comparison with the simulated scenarios.

Thanks to the new approach presented here, Lav@hazard can now be used to improve syn-eruptive nowcasting, providing near-real-time validation of the simulation input parameters and output characteristics (emplacement area, length and thickness distribution). The consequent strengthening of the strategy also improves the robustness of its application to scenario forecasting.

2. Materials and methods

The Lav@hazard web-GIS framework integrates the HOTSAT satellite monitoring system (Ganci et al., 2011a, 2011b; 2016) and the physics-based MAGFLOW model (Del Negro et al., 2008; Cappello et al., 2016b) to forecast lava flow inundation hazards. The time-varying estimates of the satellite-derived TADR (up to 4 times per hour by SEVIRI data) obtained by HOTSAT are used to drive MAGFLOW simulations in order to obtain updated lava flow scenarios in near real time. Recently the HOTSAT system, initially designed for low to moderate spatial resolution data (e.g. MODIS, AVHRR, SEVIRI) was extended to ingest higher spatial resolution satellite data (e.g. ASTER, Landsat-8, Sentinel-2) particularly relevant to retrieve detailed thermal maps of the lava flow field (Corradino et al., 2019). These thermal maps are then compared with the eruptive scenarios simulated by MAGFLOW for iterative on-line validations. This methodology, designed for the Etna volcano and validated with recent Etnean eruptions (e.g. Vicari et al., 2011b; Cappello et al., 2019), has been successfully exported to poorly monitored volcanoes (e.g. Cappello et al., 2016a).

Lav@hazard requires updated digital models of the topography over which the lava flows. This is essential since the topography can have a

Table 1
Satellite sensors ingested by Lav@Hazard. For each sensor, spatial resolution at Nadir, revisit time and possible derived products are reported.

Satellite Sensor	Spatial Resolution	Revisit Time	Derived Product
MSG-SEVIRI	3 km	15 min	Radiant Heat Flux, TADR
EOS-MODIS	1 km	12 h	Radiant Heat Flux, TADR
Landsat 8- OLI	15–30 m	7–14 days	Lava flow thermal map
Sentinel 2- MSI	10–60 m	2–3 days	Lava flow thermal map
EO-ALI	10–30 m	On demand	Lava flow thermal map
EOS-ASTER	15–90 m	On demand	DEM, Lava flow area/thickness
Pléiades-1A, -1B	0.5–2 m	On demand	DEM, Lava flow area/thickness
Doves-PlanetScope	3 m	~1 day	DEM, Lava flow area/thickness

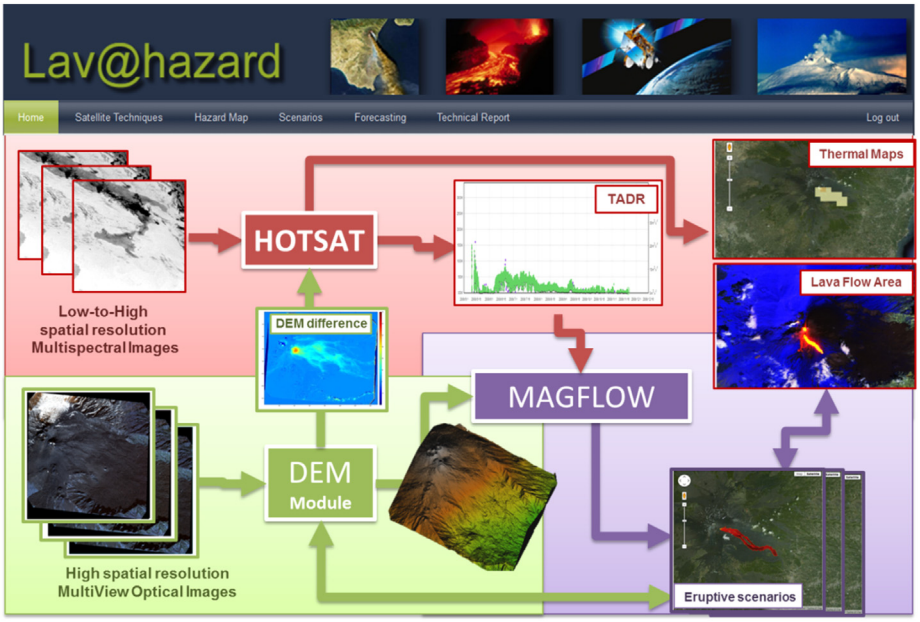

Fig. 1. Workflow of the satellite-driven modelling strategy implemented in Lav@hazard, which includes HOTSAT, MAGFLOW and the DEM Module. Thermal maps and TADRs obtained from multispectral images are used to produce and validate eruptive scenarios. DEMs derived from optical images are used to constrain volumes, as topographic base for the numerical simulations and to increase the accuracy of simulated lava flows.

significant impact on the emplacement of the flow, with direct implications on the related hazard assessment. Indeed the recency of the topographical information is more important than its level of detail (Bilotta et al., 2019).

For this reason, we included in Lav@hazard a new module (DEM Module) able to quickly produce DEMs starting from high-spatial resolution satellite data (Fig. 1). Besides providing a pre-eruptive digital topography as input parameter for MAGFLOW, the DEM module allows estimating syn- and post-eruptive bulk volumes and thickness distributions with the double objective of: (i) constraining the conversion constant from radiant heat flux to TADR performed by HOTSAT; (ii) providing validation to MAGFLOW simulated scenarios.

The DEM module relies on the free and open source MicMac software (Multi-images Correspondances, Méthodes Automatiques de Corrélation; Rupnik et al., 2017) to produce digital topography from optical satellite data acquired in stereo, tri-stero or multi-view configuration (e.g. Pléiades, PlanetScope, ASTER). As soon as syn-eruptive and/or post-eruptive stereo pairs are available, new DEMs are produced and the difference between these DEMs, including the pre-eruptive one, can be computed to retrieve areas, volumes and thickness distribution of the recent volcanic deposits. To avoid errors due to misalignment between DEMs, the co-registration method introduced by Nuth and Kääb (2011) is integrated in the DEM module.

Minimum and maximum bulk volumes of lava flows retrieved from DEMs difference are corrected for vesicles and provided to HOTSAT that compares them with the dense rock equivalent (DRE) volumes obtained from the integration of the minimum and maximum TADR curves. Since the standard uncertainty associated to HOTSAT is 30% (Ganci et al., 2013, 2016), if the DEM-derived volumes fall inside this range, the TADR curves are used for the preliminary production of lava flow scenarios. Otherwise, we apply a conservative approach by selecting the highest maximum and the lowest minimum values between the HOTSAT- and the DEM-derived volumes. Successively we rescale the TADR curves so that their integrals match these two extreme volumes by computing three constants for conversion (k_{TADR}) according to:

$$k_{TADR} = \frac{\sum \frac{1}{2}(t_i - t_{i-1})(Q_i + Q_{i-1})}{V_{DEM}} \quad (1)$$

where V_{DEM} is the volume computed from DEMs differences that will be the minimum, mean and maximum among possible values, while t_i and Q_i are the satellite passage time and the radiant heat flux computed by HOTSAT, respectively.

Our processing workflow includes:

1. Pre-eruptive DEM production from high resolution stereo pairs
2. Detection of thermal anomalies from multispectral satellite data
3. Production of thermal maps
4. Radiant heat flux estimation computed for thermally anomalous images
5. Preliminary TADR estimation by straightforward conversion of the radiant heat flux
6. Preliminary production of lava flow scenarios using TADR and pre-eruptive DEM
7. Syn-eruptive DEM production from high resolution stereo pairs
8. Calibration of TADR using DEM-derived volume
9. Refinement of lava flow scenarios using DEM-calibrated TADR
10. Validation of lava flow scenarios using higher resolution thermal and thickness maps.

The last point includes the validation between the high-to-very high satellite products, i.e. thermal map of the flow, actual lava flow area, length and thickness distribution and the same parameters computed from the simulated scenarios. Therefore the strategy relies on a two-way communication between the satellite processing and the physics-based modeling. Satellite-derived quantities (pre-eruptive DEM, DEM-constrained TADR) are used as input for the modeling framework, and the match between the simulated and DEM-derived emplacement is used to assess the accuracy of the satellite analysis itself.

3. The 2011 Nabro eruption

Nabro is a stratovolcano at the southeast end of the Danakil Alps in Eritrea, belonging to the so-called Bidu Volcanic Complex, which includes Nabro and Mallahle calderas, and Bara'Ale and Sork'Ale volcanoes (Wiart and Oppenheimer, 2005).

The 2011 eruption of Nabro volcano has been the first historical on record and one of the largest eruptions of the last decade. The previous historical eruption recorded in Eritrea was that of Dubbi volcano in 1861, located ~25 km NNE of Nabro (Wiart and Oppenheimer, 2000; Wiart et al., 2000).

At the time of the eruption, no seismic or other monitoring networks

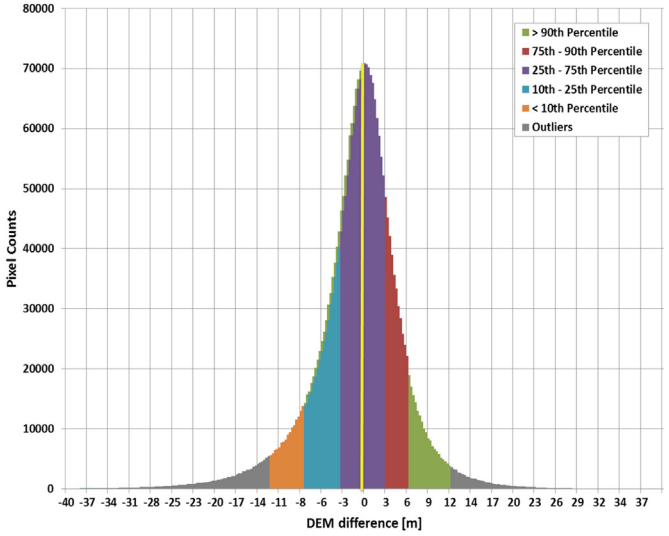

Fig. 2. Elevation change for the 2011 Nabro eruption obtained by differencing the post-eruptive DEM and PREM outside the area of the main deposits. The yellow bar peaks at -0.25 m, which is the median value. Residuals to different percentiles, as well the outliers are highlighted using different colors. (For interpretation of the references to color in this figure legend, the reader is referred to the Web version of this article.)

operated in Eritrea. For this reason the eruption began with very little warning. However, the earthquakes occurred several hours before the eruption caused a rapid spontaneous evacuation of villages within Nabro's caldera (where more than 3000 people lived) and in the surrounding of the vent opening region. Nevertheless, 7 deaths were reported in Eritrea and 31 in Ethiopia, with thousands of people displaced in temporary camps.

Starting on 12 June and lasting about 40 days, the 2011 Nabro eruption was bimodal in nature, beginning with approximately three days of explosive behavior before switching to a quieter effusive style (Goitom et al., 2015). The ash plume spread westwards over northern Africa and quickly reached a distance of more than one thousand kilometers. Moreover the eruption led to the emplacement of three lava flows and to the infilling of the pit crater inside Nabro's caldera by a tephra/lava cone. The longest lava flow was sourced by an eruptive vent located on the western side of the south-west pit rim and stretched over 15 km towards north-west in just four days. Composition of lavas ranged from trachybasalt to basaltic trachyandesite (Hamlyn et al., 2014; Goitom et al., 2015).

3.1. Digital elevation model

To map the deposits emitted during the 2011 eruption at Nabro volcano and provide an estimation of thickness distribution and volumes, we used a topographic approach relying on the difference of DEMs derived from stereoscopic ASTER (Advanced Spaceborne Thermal Emission and Reflection Radiometer) and multi-view PlanetScope images. ASTER images were processed using the MicMac ASTER (MMASTER) package that reduces overall noise compared to NASA's standard AST14DMO product (Girod et al., 2017).

Pairs of stereo images are collected by ASTER globally at a 15-m resolution in the near infrared band and consist of a nadir-pointing image (Band 3 N) and a back-looking image (Band 3B). PlanetScope images are acquired in three or four bands (Blue, Green, Red plus Near Infrared) with a ground sampling distance of ~3.7 m and a scene footprint of ~200 km^2. Even though the across track view angle of these satellites is constrained within ± 5 degrees off nadir (Ghuffar, 2018), DEM generation can be achieved thanks to the huge number of available images and exploiting the multi-view processing capabilities of MicMac.

The DEM module implemented in Lav@hazard is interfaced with MicMac including the MMASTER package. For this case study we derived six pre-eruptive DEMs from cloud-free ASTER images acquired on 30 August 2008, 5 January and 4 October 2009, 24 January and 13 March 2010, and 17 April 2011. The post-eruptive DEM was produced by using seven PlanetScope scenes acquired on 2 and 12 May 2019 with off nadir angles ranging from 0.9 to 5 degrees.

To compensate major discrepancies and achieve the maximum coherence, we first accurately coregistered the 7 DEMs applying the Nuth and Kääb (2011) algorithm that minimize both horizontal and vertical differences among the DEMs. A difference between each couple of pre-eruptive and post-eruptive DEMs was then computed and statistics on these differences were calculated outside of the deposit area. For the six combinations, we found a median value for the height difference ranging between -0.80 and 0.50 m, an InterQuartile Range (IQR) between 8.15 and 12.6 m and a Root Mean Squared Error (RMSE) between 9.6 and 14.1 m. These statistical distributions affect the quality of the thickness and volume estimations.

To improve the mapping of the outlines and thickness of deposit, as well as the estimation of the volume, we performed an intelligent fusion by deriving a pre-eruptive DEM from the six raw pre-DEMs. We integrated different available height data by considering the median value of corresponding pixels in order to discard possible blunders and errors that are present in the initial data and remove systematic errors between DEMs.

The resulting pre-eruptive median DEM (PREM) shows high accuracy and better co-registration with respect to the post-eruptive DEM. Indeed, both the IQR and RMSE for the height differences decrease to 6.07 and 6.30 m, respectively. Fig. 2 shows the distribution of terrain residuals between the post-eruptive DEM and PREM outside the areas of the deposit. The histogram, which is slightly left-skewed, peaks at the median value of -0.25 m, with 80% of the residuals falling between -7.89 and 5.85 m (10th and 90th percentile respectively), and only 6% of outliers, i.e. values differing from the mean by more than 1.5 IQRs.

The result of the difference between the post-eruptive DEM and PREM is mapped in Fig. 3, where the outlines of lava flows are clearly discriminable. By using an adaptive local threshold we outlined the four main deposits of the 2011 eruption (inset of Fig. 3): the longest lava flow, which initially travelled SW from the eruptive vent and then turned NW (*flow* α); the two smaller lava flows erupted from vents around the inner caldera (*flow* β and *flow* γ); and the new tephra and lava cone infilling the pit crater.

The main volcanological quantities (thickness, area and volume) for each of the four deposits are reported in Table 2. The maximum thickness (about 360 m) is reached at the top of the new tephra and lava cone, while more than 80% of the total area is covered by *flow* α. The mean total volume is about 577 million of cubic meters, which is again mainly due to *flow* α (more than 58%) and secondary to the volume of the cone (34%).

3.2. TADR estimation

Thermal anomalies were detected via the HOTSAT thermal monitoring system (Ganci et al., 2011, 2016) from 12 June at 20:45 GMT with SEVIRI and from 14 June at 19:15 GMT with MODIS. During the first three days, the Nabro eruption showed an explosive behavior with a thick plume that spread under the influence of wind, producing a wide tephra deposit covering about 700 square kilometers (Goitom et al., 2015). This prevented detection from satellite of the thermal anomalies associated with the active lava flow, while from 16 June the eruption moved to a more effusive style clearly observed by HOTSAT.

During the initial explosive phase, when the thermal anomaly was obscured by the tephra cloud, magma degassing rates (V_d) were reconstructed (see yellow bar in Fig. 5) from the satellite-derived estimates of SO_2 flux (Theys et al., 2013) using the following formula:

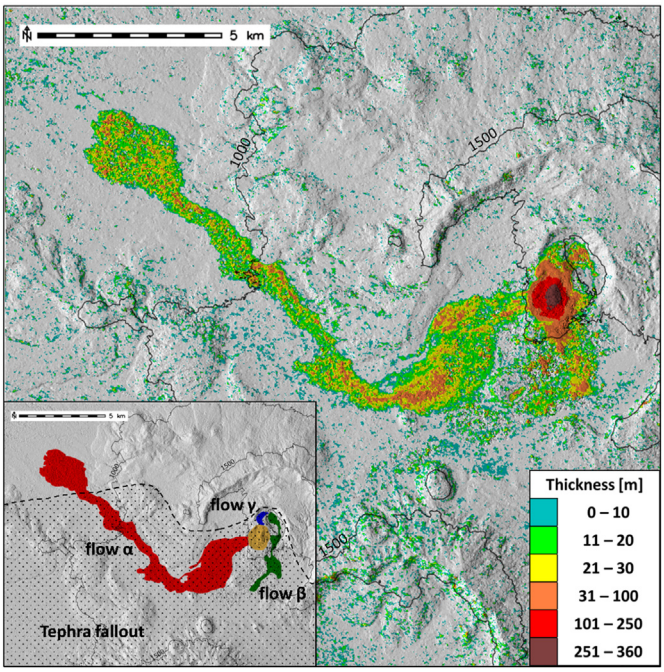

Fig. 3. Zoom of the thickness distribution of volcanic deposits obtained by differencing pre-eruptive and post-eruptive DEMs derived from ASTER and PlanetScope data, respectively. The colors indicate the positive values of deposit thickness in meters. Inset shows the four main deposits obtained by local thresholding: the longest lava flow (flow α, in red); the two smaller lava flows erupted from vents around the inner caldera (flow β, in green, and flow γ, in blue); and the tephra/lava cone infilling the pit crater (in yellow). The substantial tephra fallout that covers the SW area of Nabro volcano is also highlighted (black dots). (For interpretation of the references to color in this figure legend, the reader is referred to the Web version of this article.)

Table 2
Bulk thickness, area and bulk volume of the cone and the three lava flows identified from the difference between post- and pre-eruptive DEMs (see inset of Fig. 3). The uncertainty ranges for the estimation of the minimum and maximum volumes were estimated as the product between each area and the RMSE calculated outside the area of the deposits (i.e. 6.3 m).

Lava flow	Thickness [m]		Area [km^2]	Volume [× 10^6 m^3]		
	Mean	Max		Min	Mean	Max
Cone	156.37	361.31	1.26	188.81	196.75	204.69
flow α	18.84	66.96	17.84	223.88	336.27	448.67
flow β	18.77	77.95	2.05	25.51	38.43	51.34
flow γ	20.79	67.36	0.29	4.15	5.98	7.81
Total			21.44	442.36	577.43	712.51

$$V_d = \frac{V_s}{2[S]\rho(1-x)} \quad (2)$$

where V_S is the volume of elemental sulfur, *[S]* is the weight fraction of sulfur degassed per unit of magma, *x* is the crystal fraction and ρ is the density of magma (Allard, 1997). We used a value of 25% as mean crystal fraction, 0.3 wt % as mean original sulfur content, and 2600 kg/m^3 as density of magma (Spilliaert et al., 2006).

The TADR derived from SO_2 flux results in a cumulative volume of 136 ± 21 millions of cubic meters. This estimate is supported by the fact that the lava flow emplaced almost entirely during the first three days, as visible from MODIS images acquired on 16 June at 23:30 GMT and on 17 June at 19:45 GMT (Fig. 4).

After 16 June, the TADR was derived by the HOTSAT system by processing SEVIRI and MODIS data; the constant for conversion (k_{TADR}) from radiant heat flux to TADR was chosen following equation (1) in a way that the final DRE volume matched the volume obtained from the

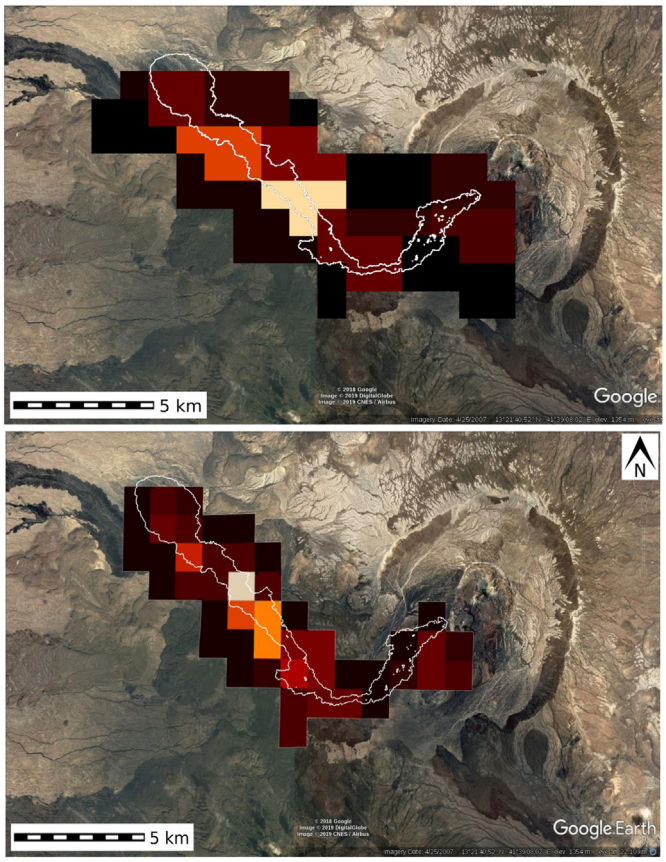

Fig. 4. Hotspot maps as obtained from MODIS images acquired on 16 June at 23:30 GMT (top) and on 17 June at 19:45 GMT (bottom). White contours represent the outlines of the lava flow fields.

DEM difference (V_{DEM}) with its range of uncertainties (Fig. 5), assuming a vesicularity of 25% (Jónsson and Xu, 2015).

The final DRE volume associated to *flow α* thus ranges between 168 and 336 millions of cubic meters.

3.3. Lava flow scenarios

We reproduced the emplacement of the longest lava flow erupted during the 2011 Nabro eruption (*flow α* in Fig. 3) by using the physics-based MAGFLOW model, which has been successfully applied in different volcanic areas both for short- and long-term hazard assessment (e.g. Del Negro et al., 2013; Cappello et al., 2015a, 2015b; 2016a; Kereszturi et al., 2014, 2016; Pedrazzi et al., 2015; Rogic et al., 2019).

MAGFLOW relies on different input parameters, including (i) the topographic information provided in the form of a DEM; (ii) the rheological properties of lava; (iii) the location of the vent(s) or fracture(s); and (iv) the flux rate over time. The MAGFLOW simulations were run on PREM, the topography derived from the six cloud-free pre-eruptive ASTER images. Rheological properties were described using a variable viscosity relationship for basaltic magma, parameterized in terms of temperature and water content. The location of vent was clearly detected in the ALI image of 29 June 2011. The flux rate over time was derived as explained in paragraph 3.2 for the first 35 days of eruption, i.e. between 12 June and 17 July 2011. In particular, using the minimum, mean and maximum TADR estimates, we simulated three eruptive scenarios.

A visual comparison between the actual flow areas and the three simulated scenarios is shown both on 19 June (7 days after the start of the eruption, Fig. 6) and at the end of the eruption (Fig. 7). On 19 June the real flow-field had attained almost 100% of its final length, as

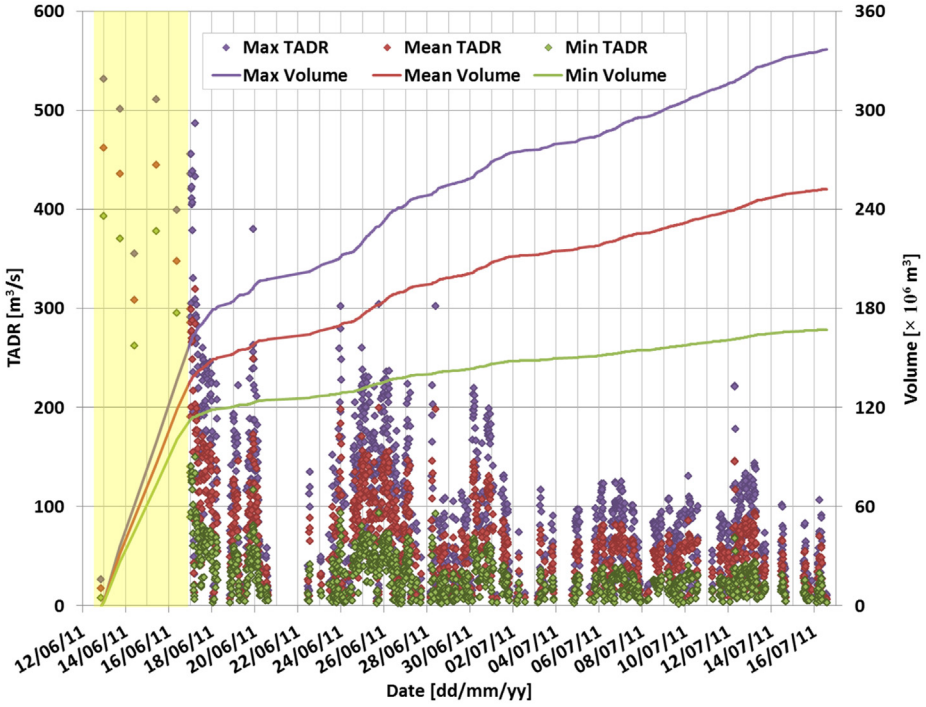

Fig. 5. Minimum (green), medium (red) and maximum (violet) estimates for TADR and cumulative volume computed in the period 12 June – 17 July 2011 by HOTSAT using MODIS and SEVIRI data. The yellow bar highlights the initial explosive phase of the eruption when TADR was derived from SO_2 flux. (For interpretation of the references to color in this figure legend, the reader is referred to the Web version of this article.)

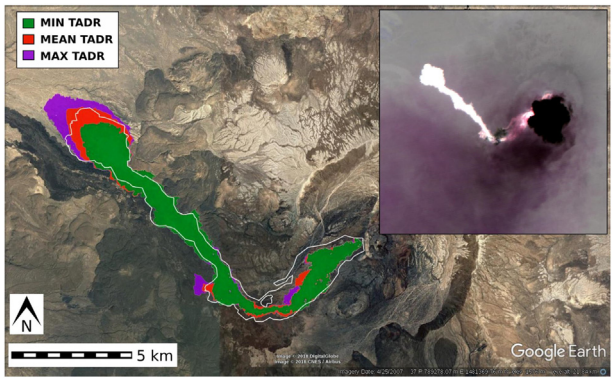

Fig. 6. Lava flow simulations run with the minimum (green), mean (red) and maximum (violet) satellite-derived TADRs on 19 June 2011. The actual lava flow field (white contour) was retrieved from the ASTER image acquired at 19:35 GMT shown in the top-right inset. (For interpretation of the references to color in this figure legend, the reader is referred to the Web version of this article.)

clearly shown by the ASTER image acquired at 19:35 GMT (inset of Fig. 6). After 19 June, *flow α* continued to thicken and widen along its length, while the front advanced ~300 m, reaching a maximum distance of 15.8 km from the main vent.

Looking at Fig. 6, the best simulated scenarios in terms of area is the one obtained using the mean TADR estimate, while the maximum TADR estimate allows to reach 65 m of maximum thickness which is close to the DEM-derived thicknesses (66.96 m, Table 2).

To determine the robustness of our results, we quantified the fitness between the real and simulated lava flows comparing the evolving lengths and areas on 19 June and 17 July (Table 3). To take into account the extent of the flows, we computed the accuracy index:

$$ACC\_2D = \sqrt{\frac{A(\text{sim} \cap \text{real})}{A(\text{sim} \cup \text{real})}} \quad (3)$$

where $A(sim \cap real)$ and $A(sim \cup real)$ are respectively the areas of the intersection and union between the simulated and actual lava flows.

To compare the thickness distribution in the simulated scenarios h_{sim} with respect to the actual one obtained by DEM difference h_{real}, a cross-correlation score over the union area was computed as:

$$CCS = \frac{\sum (h_{real} \cdot h_{sim})}{\sqrt{\sum h_{real}^2} \cdot \sqrt{\sum h_{sim}^2}} \quad (4)$$

Finally, a three dimensional accuracy index on volume distribution was computed as:

$$ACC\_3\ D = \sqrt[3]{\frac{V(\text{sim} \cap \text{real})}{V(\text{sim} \cup \text{real})}} \quad (5)$$

where $V(sim \cap real)$ and $V(sim \cup real)$ are the volumes of intersection and union, respectively.

A comparison between the ACC_2D, CCS and ACC_3D provides insights on how the simulated emplacements fit the actual areas, thicknesses and volumes.

Our indices for the Nabro eruption (Table 3) confirm that the most accurate simulation is the one driven by the mean TADR (ACC_2D = 0.83, CSS = 0.74, ACC_3D = 0.77). The simulation driven by the minimum TADR fits the actual area and thickness better than the simulation driven by the maximum TADR (0.78 vs 0.77 for ACC_2D and 0.69 vs 0.66 for CCS), which instead reproduce more successfully the actual volume distribution (0.75 vs 0.73 for ACC_3D).

4. Discussions

Satellite-derived effusion rate estimates rely on a simple formula, which relates lava discharge rate to the heat radiated per unit time from the surface of active lava flows (Wright et al., 2001). This relationship represents the state of the art in the field (Tarquini, 2017), and was also supported by recent laboratory experiments (Garel et al., 2012) proving how the heat radiated by the flow surface is proportional to the magma discharge rate after a transient time, when a steady value is reached. Despite the controversial nature of the relationship (Dragoni and Tallarico, 2009), current literature research agrees on estimating an upper and lower bound of the time-averaged discharge rate (TADR) from the instantaneous heat loss at actively flowing lava as proportional to the satellite-derived pixel-integrated spectral radiances.

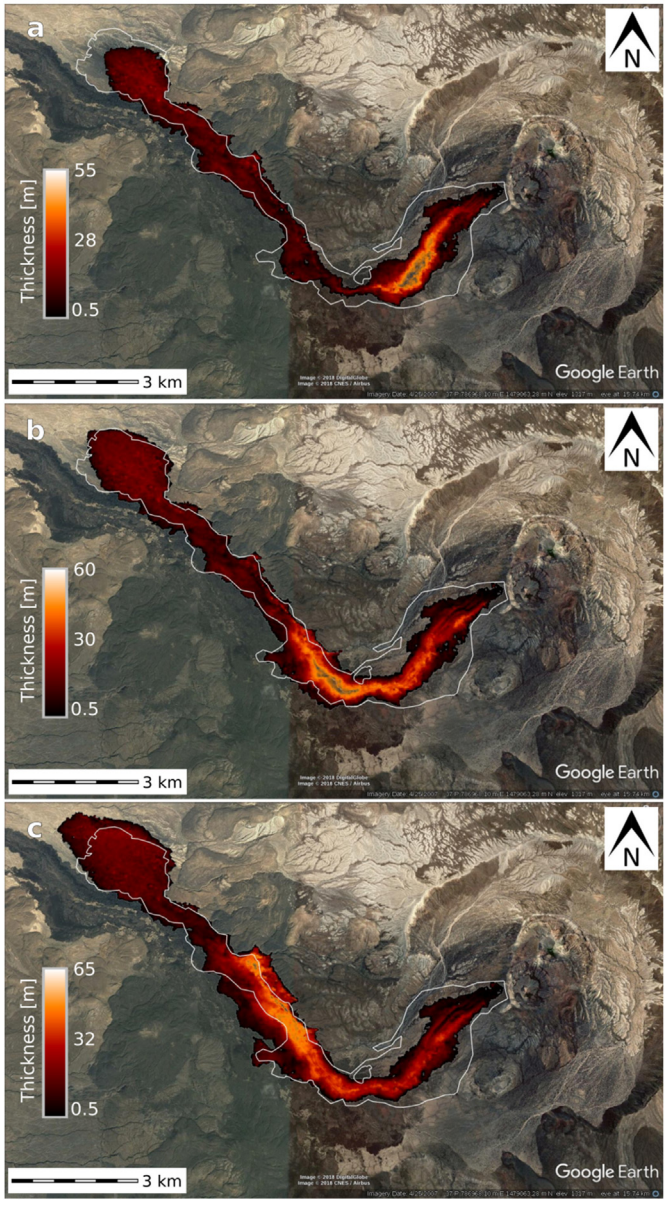

Fig. 7. Eruptive scenarios obtained by using the minimum (a), mean (b) and maximum (c) satellite-derived TADRs on 17 July 2011. The colors indicate deposit thickness in meters. Lava flow simulations were run using the following parameters: density (2600 kg m^{-3}); specific heat capacity (1150 J kg^{-1} K^{-1}); emissivity (0.9); solidification temperature (1173 K) extrusion temperature (1360 K). The actual lava flow field (white contour) was retrieved by local thresholding the difference between the pre-eruptive and post-eruptive DEMs derived from ASTER and PlanetScope data. (For interpretation of the references to color in this figure legend, the reader is referred to the Web version of this article.)

DEM differences allow us to constrain the constant (k_{TADR}) used in the conversion from radiant heat flux to TADR between 5.82×10^{7} and 1.89×10^{8} W m^{-3} s. The lower bound matches the radiant density for blocky lava flows (e.g. Reventador), and the upper bound is close to the radiant density of basaltic flows, such as Piton de la Fournaise (Coppola et al., 2013). The k_{TADR} range spanning between the two classes is consistent with the petrology of lavas with mildly alkaline composition, ranging from trachybasalt to basaltic trachyandesite found at Nabro (SiO_2 = 48–53 wt%, Goitom et al., 2015), and is in good agreement (75% overlap) with the related theoretical values between 7.54×10^{7} and 2.11×10^{8}.

Table 3
Real lava flow dimensions, and simulated lengths, areas and average thicknesses on 19 June and 17 July. ACC_2D, CCS and ACC_3D are the three indices used to quantify the goodness of fit. ACC_2D is the square root of the intersection over union areas of the simulated and actual lava flows; CCS is the cross-correlation score over union areas; ACC_3D measures the 3D accuracy index on volume distribution. CSS and ACC_3D values are not available for 19 June due to the lack of a syn-eruptive volume estimates, while the area (necessary for the computation of ACC_2D) was available from the ASTER image.

	19 June 2011			17 July 2011		
Real length [km]	15.50			15.80		
Real area [km^2]	16.07			17.84		
	MIN TADR	MEAN TADR	MAX TADR	MIN TADR	MEAN TADR	MAX TADR
Simulated length [km]	15.22	16.02	16.08	15.51	16.06	16.99
Simulated area [km^2]	12.43	14.67	16.99	13.36	16.83	19.73
Simulated average thickness [m]	9.88	10.75	11.32	12.52	15.27	17.07
ACC_2D	0.78	0.84	0.80	0.78	0.83	0.77
CCS	N/A	N/A	N/A	0.69	0.74	0.66
ACC_3D	N/A	N/A	N/A	0.73	0.77	0.75

Typical basaltic lava parameters used to convert satellite thermal data to TADR (Harris et al., 2000, 2007) provide a conversion constant of about 6.8×10^{8}. Comparing the volume obtained using this standard constant with the one from DEM difference, we get an underestimation up to 70%. This is not surprising; indeed, by comparing volume estimates retrieved from thermal data and topographic mapping on other volcanoes, differences up to 140% can be found. This is the case, for example, of the 2014 Stromboli eruption, where estimate difference ranges between 80% and 141% (compare Di Traglia et al., 2018 and Zaksek et al., 2015) or of the Fogo 2014-15 eruption, where the difference is between 54% and 72% (compare Bagnardi et al., 2016 and Cappello et al., 2016a). These gaps can be ascribed to several factors, such as the presence of lava tubes (Fogo) or overflows to the sea (Stromboli); in general, they demonstrate the importance of introducing a real-time check with the topographic monitoring of the deposits.

By using the TADR curves of Fig. 5, we estimate an average effusion rate of about 250 ± 50 m^{3}s^{-1} for the *flow α* on 19 June. Assuming an emplacement style dominated by cooling-limited conditions and applying the empirical formula of Calvari and Pinkerton (1998), which relates the maximum flow length to effusion rate, emplacement time and mean ground slope, we found a maximum length between 14.5 and 16 km that is perfectly in agreement with the actual length (15.5 km) as retrieved from the ASTER image on 19 June (Table 3). Moreover, considering the actual flow area (16.07 km^2) and the satellite-derived volume at the same time, we found an average flow thickness of about 9.7 ± 2 m, which is consistent with the formation of the lava flow field and the final average thickness (see Table 2).

Lava flow simulation results give substance to the TADR curves, particularly with the mean TADR, which gives the best scenario in terms of both length and thickness distribution. This shows that the lava flow is likely to have reached 10.5 km in one day and the maximum length of 16.06 km on 20 June (Fig. 8), giving a maximum speed of ~0.44 km/h.

Obviously, the accuracy of our results depends on the quality of input parameters in the MAGFLOW model, including information on magma properties, the resolution of the pre-eruptive DEM and the shape of the effusion rate curves (Bilotta et al., 2012, 2019).

The main difference between the actual and the simulated scenarios occurs in the area more proximal to the eruptive vent. This mismatching could be due to the emptying of the flow interior at the flow margins (Calvari et al., 2018) and/or to the solidification of the initial

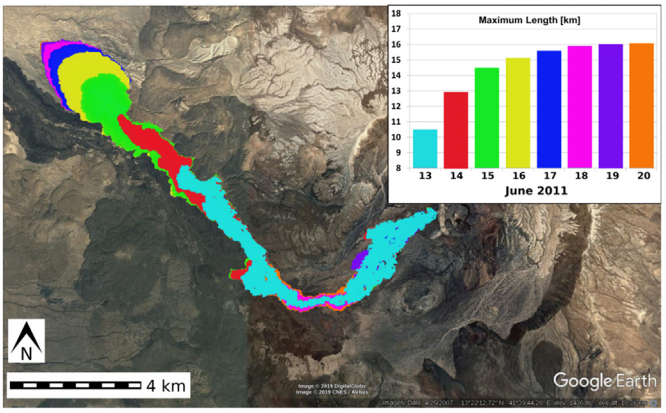

Fig. 8. MAGFLOW scenarios with the mean TADR during the first 8 days of eruption. Colors represent the scenario at the end of each day. The inset shows the maximum length reached at each day. (For interpretation of the references to color in this figure legend, the reader is referred to the Web version of this article.)

portion of the flow that acted as a barrier to the subsequent overlapping flows spreading in the surrounding areas and widening the actual emplacement.

5. Conclusions

Due to the remote location of the Nabro volcano and the lack of data from monitoring networks at the time of the eruption, satellite remote sensing gives the first global view of the event, providing insights on its evolution over time. Here we used numerical modeling and high spatial resolution satellite data (i.e. EO-ALI, ASTER, PlanetScope) to track the path and velocity of lava flows and to reconstruct the pre- and post-eruptive topographies in order to quantify the total bulk volume emitted. High temporal resolution images (i.e. SEVIRI and MODIS) were exploited by HOTSAT to estimate the TADR and assess the DRE lava volume constrained by the topographic approach. The pre-eruptive topography and TADR were then provided as input to MAGFLOW to produce eruptive scenarios, offering further insights into the eruption and emplacement dynamics.

We remark that, while some of the data is used both for input and for validation, our approach is not purely circular: its strength stems from the combination of previously validated techniques and models (HOTSAT for radiance flux estimation, MAGFLOW for lava flow simulation) and new methods (*a posteriori* DEM-based TADR constraining). In particular, the DEM-derived volumes are only used to constraint the magnitude of the TADR, while its trend over time is derived from the analysis of the thermal imagery, and the trend itself is known to be at least as important as the magnitude of the mass flux in determining the area, length and thickness distribution of a lava flow emplacement (Bilotta et al., 2012), which are the parameters we use in the validation process.

The number of techniques devoted to topographic monitoring by processing high-resolution optical satellite images in stereo or tri-stereo configuration is exponentially increasing, following the growing number of remote sensors and data available. For example, Planet Labs have recently launched a large constellation of miniature satellites called Doves (nearly 300, of which 150 are currently active) with the capability of imaging the entire Earth surface every day at 3–5 m spatial resolution (e.g. PlanetScope, Rapideye). Such a huge number of satellites increases the possibility to have multi-view acquisitions and hence to use them for daily topography update (Ghuffar, 2018).

The presented strategy provides important constraints in the conversion between radiant heat flux and TADR, and demonstrates the powerful merging capability of multi-platform remote sensing data, representing another step towards a global system for volcano warning and hazard monitoring, especially in comparatively remote regions where local ground-based sensor networks are limited or lacking.

Description of author's responsibilities

GG and AC mainly wrote the manuscript with contributions from all the authors. GG conceived the idea and processed satellite data. AC computed DEM differences and performed lava flow simulations. GB performed the statistical analysis. CDN coordinated the research. All authors contributed to the ideas, writing, and discussion.

Acknowledgments

This work was developed at the Laboratory of Technologies for Volcanology (TecnoLab) at INGV in Catania (Italy). We gratefully acknowledge funding support from the DPC-INGV 2012–2021 agreement and from ATHOS Research Programme. Thanks are due to European Organisation for the Exploitation of Meteorological Satellites (EUMETSAT) for SEVIRI data (www.eumetsat.int) and to National Aeronautics and Space Administration (NASA) for MODIS data (modis.gsfc.nasa.gov). Landsat 8 OLI and EO-1 ALI images are courtesy of the U.S. Geological Survey (earthexplorer.usgs.gov). ASTER data are courtesy of NASA Earthdata (https://earthdata.nasa.gov/). We would like to thank Planet Labs, Inc. for providing the PlanetScope imagery through the Education and Research Program. We are grateful to Sajid Ghuffar for helping in the choice of the best combination of PlanetScope images. We thank the Editor-in-Chief Jing M. Chen, the Associate Editor Joseph Awange, Federico Di Traglia and two anonymous reviewers for their help in improving the clarity of the manuscript.

References

Allard, P., 1997. Endogenous magma degassing and storage at Mount Etna. Geophys. Res. Lett. 24, 2219–2222.

Bagnardi, M., González, P.J., Hooper, A., 2016. High-resolution digital elevation model from tri-stereo Pleiades-1 satellite imagery for lava flow volume estimates at Fogo Volcano. Geophys. Res. Lett. 43 (12), 6267–6275.

Bilotta, G., Cappello, A., Hérault, A., Del Negro, C., 2019. Influence of topographic data uncertainties and model resolution on the numerical simulation of lava flows. Env. Model. Soft. 112, 1–15. https://doi.org/10.1016/j.envsoft.2018.11.001.

Bilotta, G., Cappello, A., Hérault, A., Vicari, A., Russo, G., Del Negro, C., 2012. Sensitivity analysis of the MAGFLOW Cellular Automaton model for lava flow simulation. Environ. Model. Softw 35, 122–131. https://doi.org/10.1016/j.envsoft.2012.02.015.

Calvari, S., Ganci, G., Victória, S.S., Hernandez, P.A., Perez, N.M., Barrancos, J., Alfama, V., Dionis, S., Cabral, J., Cardoso, N., Fernandes, P., Melian, G., Pereira, J.M., Semedo, H., Padilla, G., Rodriguez, F., 2018. Satellite and ground remote sensing techniques to trace the hidden growth of a lava flow field: the 2014–2015 effusive eruption at Fogo volcano (Cape Verde). Remote Sens. 10, 1115. https://doi.org/10.3390/rs10071115.

Calvari, S., Pinkerton, H., 1998. Formation of lava tubes and extensive flow field during the 1991-1993 eruption of Mount Etna. J. Geophys. Res. 103, 27291–27301.

Cappello, A., Geshi, N., Neri, M., Del Negro, C., 2015a. Lava flow hazards-An impending threat at Miyakejima volcano, Japan. J. Volcanol. Geotherm. Res. 308, 1–9. https://doi.org/10.1016/j.jvolgeores.2015.10.005.

Cappello, A., Zanon, V., Del Negro, C., Ferreira, T.J.L., Queiroz, M.G.P.S., 2015b. Exploring lava-flow hazards at pico island, azores archipelago (Portugal). Terra. Nova 27 (2), 156–161. https://doi.org/10.1111/ter.12143.

Cappello, A., Ganci, G., Calvari, S., Pérez, N.M., Hernández, P.A., Silva, S.V., Cabral, J., Del Negro, C., 2016a. Lava flow hazard modeling during the 2014-2015 Fogo eruption, Cape Verde. J. Geophys. Res. Solid Earth 121. https://doi.org/10.1002/2015JB012666.

Cappello, A., Hérault, A., Bilotta, G., Ganci, G., Del Negro, C., 2016b. MAGFLOW: a Physics-Based Model for the Dynamics of Lava-Flow Emplacement, vol. 426. Geological Society of London, Special Publications, pp. 357–373. https://doi.org/10.1144/SP426.16.

Cappello, A., Ganci, G., Bilotta, G., Hérault, A., Zago, V., Del Negro, C., 2019. Satellite-driven modeling approach for monitoring lava flow hazards during the 2017 Etna eruption. Ann. Geophys. 61. https://doi.org/10.4401/ag-7792.

Coppola, D., Laiolo, M., Piscopo, D., Cigolini, C., 2013. Rheological control on the radiant density of active lava flows and domes. J. Volcanol. Geotherm. Res. 249, 39–48.

Corradino, C., Ganci, G., Bilotta, G., Cappello, A., Del Negro, C., Fortuna, L., 2019. Smart decision support systems for volcanic applications. Energies 12 (7), 1216. https://doi.org/10.3390/en12071216.

Corsaro, R.A., Pompilio, M., 2004. Buoyancy-controlled eruption of magmas at Mt Etna.

Terra. Nova 16 (1), 16–22. https://doi.org/10.1046/j.1365-3121.2003.00520.x.
Darmawan, H., Walter, T.R., Brotopuspito, K.S., Nandaka, I.G.M.A., 2018. Morphological and structural changes at the Merapi lava dome monitored in 2012–15 using unmanned aerial vehicles (UAVs). J. Volcanol. Geotherm. Res. 349, 256–267.
Del Negro, C., Cappello, A., Ganci, G., 2016. Quantifying lava flow hazards in response to effusive eruption. Bull. Geol. Soc. Am. 128, 1–13. https://doi.org/10.1130/B31364.1.
Del Negro, C., Cappello, A., Neri, M., Bilotta, G., Herault, A., Ganci, G., 2013. Lava flow hazards at Mount Etna: constraints imposed by eruptive history and numerical simulations. Sci. Rep. 3, 3493. https://doi.org/10.1038/srep03493.
Del Negro, C., Fortuna, L., Herault, A., Vicari, A., 2008. Simulations of the 2004 lava flow at Etna volcano by the MAGFLOW Cellular Automata model. Bull. Volcanol. 70, 805–812. https://doi.org/10.1007/s00445-007-0168-8. 0258-8900.
Di Traglia, F., Calvari, S., D'Auria, L., Nolesini, T., Bonaccorso, A., Fornaciai, A.,, et al., 2018. The 2014 effusive eruption at Stromboli: new insights from in situ and remote-sensing measurements. Remote Sens. 10 (12), 2035.
Dragoni, M., Tallarico, A., 2009. Assumptions in the evaluation of lava effusion rates from heat radiation. Geophys. Res. Lett. 36, L08302. https://doi.org/10.1029/2009GL037411.
Favalli, M., Fornaciai, A., Nannipieri, L., Harris, A., Calvari, S., Lormand, C., 2018. UAV-based remote sensing surveys of lava flow fields: a case study from Etna's 1974 channel-fed lava flows. Bull. Volcanol. 80 (3), 29.
Fornaciai, A., Behncke, B., Favalli, M., Neri, M., Tarquini, S., Boschi, E., 2010. Detecting short-term evolution of Etnean scoria cones: a LIDAR-based approach. Bull. Volcanol. 72 (10), 1209–1222.
Ganci, G., Vicari, A., Bonfiglio, S., Gallo, G., Del Negro, C., 2011a. A texton-based cloud detection algorithm for MSG-SEVIRI multispectral images. Geomatics, Nat. Hazards Risk 2, 279–290. https://doi.org/10.1080/19475705.2011.578263.
Ganci, G., Vicari, A., Fortuna, L., Del Negro, C., 2011b. The HOTSAT volcano monitoring system based on a combined use of SEVIRI and MODIS multispectral data. Ann. Geophys. 54, 5. https://doi.org/10.4401/ag-5338. 2011.
Ganci, G., Vicari, A., Cappello, A., Del Negro, C., 2012. An emergent strategy for volcano hazard assessment: from thermal satellite monitoring to lava flow modeling. Remote Sens. Environ. 119, 197–207. https://doi.org/10.1016/j.rse.2011.12.021.
Ganci, G., Cappello, A., Zago, V., Bilotta, G., Hérault, A., Del Negro, C., 2019. 3D Lava flow mapping of the 17–25 May 2016 Etna eruption using tri-stereo optical satellite data. Ann. Geophys. 62 (2). https://doi.org/10.4401/ag-7875. V0220.
Ganci, G., James, M.R., Calvari, S., Del Negro, C., 2013. Separating the thermal fingerprints of lava flows and simultaneous lava fountaining using ground-based thermal camera and SEVIRI measurements. Geophys. Res. Lett. 40, 5058–5063.
Ganci, G., Bilotta, G., Cappello, A., Hérault, A., Del Negro, C., 2016. HOTSAT: a multiplatform system for the satellite thermal monitoring of volcanic activity. Geological Society of London, Special Publications 426, 207–221. https://doi.org/10.1144/SP426.21.
Ganci, G., Cappello, A., Bilotta, G., Hérault, A., Zago, V., Del Negro, C., 2018. Mapping volcanic deposits of the 2011–2015 Etna eruptive events using satellite remote sensing. Front. Earth Sci. 6, 83. https://doi.org/10.3389/feart.2018.00083.
Ganci, G., Cappello, A., Bilotta, G., Hérault, A., Zago, V., Del Negro, C., 2019b. 3D Lava flow mapping at Etna volcano from Pléiades-derived DEM differences. PANGAEA. https://doi.org/10.1594/PANGAEA.899176.
Garel, F., Kaminski, E., Tait, S., Limare, A., 2012. An experimental study of the surface thermal signature of hot subaerial isoviscous gravity currents: implications for thermal monitoring of lava flows and domes. J. Geophys. Res. 117, B02205.
Ghuffar, S., 2018. DEM generation from multi satellite PlanetScope imagery. Remote Sens. 10 (9), 1462. https://doi.org/10.3390/rs10091462. 2018.
Girod, L., Nuth, C., Kääb, A., Mcnabb, R., Galland, O., 2017. MMASTER: improved ASTER DEMs for elevation change monitoring. Remote Sens. 9, 704. https://doi.org/10.3390/rs9070704.
Goitom, B., Oppenheimer, C., Hammond, J.O., Grandin, R., Barnie, T., Donovan, A., Ogubazghi, G., Yohannes, E., Kibrom, G., Kendall, G.M., Carn, S., Fee, D., Sealing, C., Keir, D., Ayele, A., Blundy, J., Hamlyn, J., Wright, T., Berhe, S., 2015. First recorded eruption of Nabro volcano, Eritrea, 2011. Bull. Volcanol. 77, 85. https://doi.org/10.1007/s00445-015-0966-3.
Hamlyn, J.E., Keir, D., Wright, T.J., Neuberg, J.W., Goitom, B., Hammond, J.O., Grandin, R., 2014. Seismicity and subsidence following the 2011 Nabro eruption, Eritrea: insights into the plumbing system of an off-rift volcano. J. Geophys. Res.: Solid Earth 119 (11), 8267–8282.
Harris, A.J.L., Murray, J.B., Aries, S.E., Davies, M.A., Flynn, L.P., Wooster, M.J., Wright, R., Rothery, D.A., 2000. Effusion rate trends at Etna and Krafla and their implications for eruptive mechanisms. J. Volcanol. Geotherm. Res. 102, 237–270.
Harris, A.J.L., Dehn, J., Calvari, S., 2007. Lava effusion rate definition and measurement: a review. Bull. Volcanol. 70, 1–22.
Harris, A.J.L., Favalli, M., Steffke, A., Fornaciai, A., Boschi, E., 2010. A relation between lava discharge rate, thermal insulation, and flow area set using lidar data. Geophys. Res. Lett. 37, L20308. https://doi.org/10.1029/2010GL044683.
Herault, A., Vicari, A., Ciraudo, A., Del Negro, C., 2009. Forecasting lava flow hazard during the 2006 Etna eruption: using the Magflow cellular automata model. Comput. Geosci. 35 (5), 1050–1060.
Jónsson, S., Xu, W., 2015. Volcanic eruptions in the southern red sea during 2007–2013. In: The Red Sea. Springer Berlin Heidelberg, pp. 175–186. https://doi.org/10.1007/978-3-662-45201-1_10.
Kereszturi, G., Cappello, A., Ganci, G., Procter, J., Németh, K., Del Negro, C., Cronin, S.J., 2014. Numerical simulation of basaltic lava flows in the Auckland Volcanic Field, New Zealand – implication for volcanic hazard assessment. Bull. Volcanol. 76, 879. https://doi.org/10.1007/s00445-014-0879-6.
Kereszturi, G., Nemeth, K., Vioufti, M.R., Cappello, A., Murcia, H., Ganci, G., Del Negro, C., Procter, J., Zahran, H.M.A., 2016. Emplacement conditions of the 1256 AD Al-Madinah lava flow field in Harrat Rahat, Kingdom of Saudi Arabia—insights from surface morphology and lava flow simulations. J. Volcanol. Geotherm. Res. 309, 14–30. https://doi.org/10.1016/j.jvolgeores.2015.11.002.
Müller, D., Walter, T.R., Schöpa, A., Witt, T., Steinke, B., Gudmundsson, M.T., Dürig, T., 2017. High-resolution digital elevation modeling from TLS and UAV campaign reveals structural complexity at the 2014/2015 Holuhraun eruption site, Iceland. Front. Earth Sci. 5, 59.
Neri, M., Mazzarini, F., Tarquini, S., Bisson, M., Isola, I., Behncke, B., et al., 2008. The changing face of Mount Etna's summit area documented with Lidar technology. Geophys. Res. Lett. 35, L09305. https://doi.org/10.1029/2008GL033740.
Neri, M., De Maio, M., Crepaldi, S., Suozzi, E., Lavy, M., Marchionatti, Calvari, S., Buongiorno, M.F., 2017. Topographic maps of mount etna's summit craters, updated to december 2015. J. Maps. https://doi.org/10.1080/17445647.2017.1352041.
Nuth, C., Kääb, A., 2011. Co-registration and bias corrections of satellite elevation data sets for quantifying glacier thickness change. Cryosphere 5, 271–290. https://doi.org/10.5194/tc-5-271-2011.
Pedrazzi, D., Cappello, A., Zanon, V., Del Negro, C., 2015. Impact of effusive eruptions from the eguas-carvao fissure system, sao miguel island, azores archipelago (Portugal). J. Volcanol. Geotherm. Res. 291, 1–13. https://doi.org/10.1016/j.jvolgeores.2014.12.012.
Rogic, N., Cappello, A., Ferrucci, F., 2019. Role of emissivity in lava flow 'Distance-to-Run' estimates from satellite-based volcano monitoring. Remote Sens. 11 (6), 662. https://doi.org/10.3390/rs11060662.
Rupnik, E., Daakir, M., Pierrot Deseilligny, M., 2017. MicMac – a free, open-source solution for photogrammetry. Open geospatial data, softw. stand. 2, 14. https://doi.org/10.1186/s40965-017-0027-2.
Scifoni, S., Coltelli, M., Marsella, M., Proietti, C., Napoleoni, Q., Vicari, A., Del Negro, C., 2010. Mitigation of lava flow invasion hazard through optimized barrier configuration aided by numerical simulation: the case of the 2001 Etna eruption. J. Volcanol. Geotherm. Res. 192, 16–26. https://doi.org/10.1016/j.jvolgeores.2010.02.002. 0377-0273.
Slatcher, N., James, M.R., Calvari, S., Ganci, G., Browning, J., 2015. Quantifying effusion rates at active volcanoes through integrated time-lapse laser scanning and photography. Remote Sens. 7, 14967–14987. https://doi.org/10.3390/rs71114967.
Spampinato, L., Ganci, G., Hernández, P.A., Calvo, D., Tedesco, D., Pérez, N.M., Calvari, S., Del Negro, C.D., Yalire, M.M., 2013. Thermal insights into the dynamics of Nyiragongo lava lake from ground and satellite measurements. J. Geophys. Res. Solid Earth 118, 5771–5784. https://doi.org/10.1002/2013JB010520.
Spilliaert, N., Allard, P., Metrich, N., Sobolev, A.V., 2006. Melt inclusion record of the conditions of ascent, degassing, and extrusion of volatile-rich alkali basalt during the powerful 2002 flank eruption of Mount Etna (Italy). J. Geophys. Res. Solid Earth 111.
Tarquini, S., 2017. A review of mass and energy flow through a lava flow system: insights provided from a non-equilibrium perspective. Bull. Volcanol. 79 (8), 64.
Theys, N., Campion, R., Clarisse, L., Brenot, H., van Gent, J., Dils, B., Corradini, S., Merucci, L., Coheur, P.-F., Van Roozendael, M., Hurtmans, D., Clerbaux, C., Tait, S., Ferrucci, F., 2013. Volcanic SO_2 fluxes derived from satellite data: a survey using OMI, GOME-2, IASI and MODIS. Atmos. Chem. Phys. 13, 5945–5968. https://doi.org/10.5194/acp-13-5945-2013.
Turner, N.R., Perroy, R.L., Hon, K., 2017. Lava flow hazard prediction and monitoring with UAS: a case study from the 2014–2015 Pāhoa lava flow crisis, Hawaii. J Appl Volcanol 6 (1), 17.
Vicari, A., Bilotta, G., Bonfiglio, S., Cappello, A., Ganci, G., Herault, A., Rustico, E., Gallo, G., Del Negro, C., 2011a. LAV@HAZARD: a web-GIS interface for volcanic hazard assessment. Ann. Geophys. 54, 662–670. https://doi.org/10.4401/ag-5347.
Vicari, A., Ciraudo, A., Del Negro, C., Hérault, A., Fortuna, L., 2009. Lava flow simulations using discharge rates from thermal infrared satellite imagery during the 2006 Etna eruption. Nat. Hazards 50, 539–550. https://doi.org/10.1007/s11069-008-9306-7.
Vicari, A., Ganci, G., Behncke, B., Cappello, A., Neri, M., Del Negro, C., 2011b. Near-real-time forecasting of lava flow hazards during the 12-13 January 2011 Etna eruption. Geophys. Res. Lett. 38, 0094–8276. https://doi.org/10.1029/2011GL047545.
Wiart, P., Oppenheimer, C., Francis, P., 2000. Eruptive history of Dubbi volcano, Northeast Afar (Eritrea), revealed by optical and SAR image interpretation. Int. J. Remote Sens. 21, 911–936.
Wiart, P., Oppenheimer, C., 2005. Large magnitude silicic volcanism in north Afar: the Nabro volcanic range and Ma'alalta volcano. Bull. Volcanol. 67, 99–115.
Wooster, M.J., Zhukov, B., Oertel, D., 2003. Fire radiative energy for quantitative study of biomass burning: derivation from the BIRD experimental satellite and comparison to MODIS fire products. Remote Sens. Environ., 1410 86 (1), 83–107.
Wright, R., Blake, S., Harris, A.J.L., Rothery, D.A., 2001. A simple explanation for the space-based calculation of lava eruption rates. Earth Planet. Sci. Lett. 192, 223–233.
Zakšek, K., Hort, M., Lorenz, E., 2015. Satellite and ground based thermal observation of the 2014 effusive eruption at Stromboli volcano. Remote Sens. 7 (12), 17190–17211.